APS physics

CHORUS

This is the accepted manuscript made available via CHORUS. The article has been published as:

Bowen-York-type initial data for binaries with neutron stars

Michael Clark and Pablo Laguna

Phys. Rev. D **94**, 064058 — Published 21 September 2016

DOI: 10.1103/PhysRevD.94.064058

Bowen-York Type Initial Data for Binaries with Neutron Stars

Michael Clark[1] and Pablo Laguna[1]

[1] *Center for Relativistic Astrophysics and School of Physics*
Georgia Institute of Technology, Atlanta, GA 30332

A new approach to construct initial data for binary systems with neutron star components is introduced. The approach is a generalization of the puncture initial data method for binary black holes based on Bowen-York solutions to the momentum constraint. As with binary black holes, the method allows setting orbital configurations with direct input from post-Newtonian approximations and involves solving only the Hamiltonian constraint. The effectiveness of the method is demonstrated with evolutions of double neutron star and black hole – neutron star binaries in quasi-circular orbits.

PACS numbers:

I. INTRODUCTION

Compact object binaries with black hole (BH) and neutron star (NS) components are main targets of gravitational wave (GW) observations. GWs from binary black holes (BBHs) have been recently detected by the Laser Interferometer Gravitational Wave Observatory (LIGO), first detection in the transient event GW150914 [1] and second detection in the transient event GW151226 [2]. As advanced LIGO reaches designed sensitivity, GWs from double neutron star (DNS) and black hole - neutron star (BH-NS) binaries will very likely also be detected. Not surprisingly, numerical relativity (NR) simulations played an important role in the analysis of the GW150914 and GW151226 events. Specifically, best fits of a NR waveform to the data were included in the detection paper [1]. The papers on parameter estimation [3] and tests of general relativity [4] mentioned that results from BBH simulations were involved in the construction of the phenomenological and effective-one-body waveform models used in the analysis. The same applies to the paper on the burst-type analysis of GW150914 [5].

As with GW150914 and GW151226, our ability to distinguish in future GW observations whether a signal originated from a BBH, a DNS, or a BH-NS binary will rely on waveform templates with input from NR. This would be particularly important during the last orbits and coalescence of the binary, where strong dynamical gravity is the most relevant. In this regard, NR simulations of binary systems with NS companions have experience a boost in accuracy and sophistication. These days the simulations routinely include realistic equations of state, magnetic fields, and radiation. But the predicting power of simulations not only hinges on the multi-physics included. The degree to which the initial data represent an accurate astrophysical setting is also crucial. Another important aspect connected to the initial data is the capability to explore a vast range of scenarios. And for this to happen, one needs initial data methodologies that are computationally inexpensive. In BBH simulations, low-cost and efficient methods to construct astrophysically relevant initial data have been available for some time [6–8], which is not exactly the case for binaries with NSs.

A popular method to construct initial data representing a binary system in a quasi-circular orbit is the conformal thin sandwich approach. The method has been used for BBHs by Grandclément et al. [9], for DNS by Gourgoulhon et al. [10], and for BH-NS binaries by Etienne et al. [11]. The key in those studies was the identification of a helical Killing vector field, so the initial data are approximately time-symmetric, ensuring that the compact objects are in a quasi-circular orbit. The conformal thin sandwich approach requires solving a set of five elliptic equations for the conformal factor, lapse function and shift vector [12–14]. Many groups have used the Lorene code from the Meudon group [15, 16] for this purpose, and other groups have developed their own infrastructure [17–23].

This paper introduces a new approach to construct initial data for binary systems with NS components. The method is simpler than the thin sandwich one, and it has a computational cost similar to that of the BBH puncture method. In the BBH puncture approach [24], one only solves the Hamiltonian constraint for the conformal factor. The solution to the momentum constraint is given by the Bowen-York extrinsic curvature [25]. Each initial data set is then fully specified by the masses, spins and momenta of the BHs, and their separation. All of these parameters are obtained from integrating the post-Newtonian (PN) equations of motion. The integration starts at large separations and ends at the separation where the NR initial data are constructed. This method is known to yield initial data suitable for stitching together NR and PN evolutions.

The new initial data proposal in this paper recycles most of the elements of the puncture BBH initial data, including the ability of specifying masses, spins and momenta of the compact objectss from PN approximations. The key step is constructing an extrinsic curvature for NSs similar to the Bowen-York for BHs. The paper is organized as follows: In Section II, we provide a quick review of York's initial data formulation. Section III reintroduces the Bowen-York extrinsic curvature for arbitrary, spherically symmetric momentum sources. Section IV discusses an approach to specifying the matter source functions for the initial data equations. Sec-

tion V summarizes the steps to construct initial data. Section VI reviews the stellar model we will use to represent NSs. Section VII presents tests with an isolated NS. Results of simulations of DNS and BH-NS binaries are presented in Section VIII. Paper ends with conclusions in Section IX.

The numerical simulations in the present work were carried out with our Maya code [26–31]. The code is based on the BSSN formulation of the Einstein equations [32] and the moving puncture gauge condition [33, 34]. Maya is very similar to the Einstein code in the Einstein Toolkit [35]. That is, it operates under the Cactus infrastructure [36], with Carpet providing mesh refinements [37] and thorns (modules) generated by the package Kranc [38].

II. INITIAL DATA AT A GLANCE

When the Einstein equations of general relativity are viewed as an initial value problem, the initial data are not completely freely specifiable. They must satisfy the Hamiltonian and momentum constraints:

$$R + K^2 - K_{ij}K^{ij} = 16\,\pi\,\rho_{\rm H} \quad (1)$$
$$\nabla_j (K^{ij} - \gamma^{ij} K) = 8\,\pi\, S^i\,. \quad (2)$$

Above, γ_{ij} and K_{ij} are the metric and extrinsic curvature of the space-like hypersurfaces in the foliation. In addition, R is the Ricci scalar, and ∇_i denotes covariant differentiation associated with γ_{ij}. The sources $\rho_{\rm H}$ and S^i are obtained from the stress-energy tensor T_{ab} as follows:

$$\rho_{\rm H} = n^a n^b T_{ab} \quad (3)$$
$$S^i = -\gamma^{ib} n^c T_{bc}\,, \quad (4)$$

where n^a is the unit normal to the space-like hypersurfaces. We are using units in which $G = c = 1$. Latin indices from the beginning of the alphabet denote spacetime indices and from the middle of the alphabet spatial indices. For a perfect fluid, the stress-energy tensor reads

$$\begin{aligned} T_{ab} &= (\rho + p)\, u_a u_b + p\, g_{ab} \\ &= \rho_0\, h\, u_a u_b + p\, g_{ab}\,, \end{aligned} \quad (5)$$

where $h = 1+\epsilon+p/\rho_0$ is the enthalpy, p is the pressure, u^a is the 4-velocity of the fluid, ρ_0 is the rest-mass density, ϵ is the specific internal energy density, and $\rho = \rho_0(1+\epsilon)$ is the total mass-energy density. In terms of these quantities, the sources in the Hamiltonian and momentum constraints read:

$$\rho_{\rm H} = (\rho + p)\, W^2 - p = \rho_0\, h\, W^2 - p \quad (6)$$
$$S^i = (\rho + p) W u^i = \rho_0\, h\, W u^i \quad (7)$$

where $W = -n_a u^a$ is the Lorentz factor between normal and fluid observers.

Since the initial data consist of the set $\{\gamma_{ij}, K_{ij}, \rho_{\rm H}, S^i\}$, the pressing issue is to identify which "pieces" in these data are to be fixed by the constraint Eqs. (1) and (2), and which data are indeed freely specifiable.

Motivated by the work of Lichnerowicz [12], York and collaborators [39] developed an elegant way of achieving this task. The basis of this approach is using conformal transformations and transverse-traceless decompositions to single out the four quantities fixed by the constraint equations. One quantity, the conformal factor Φ, is obtained from the spatial metric by applying the conformal transformation:

$$\gamma_{ij} = \Phi^4 \bar\gamma_{ij}\,. \quad (8)$$

The remaining three quantities, the components of the vector $\mathcal{W}^i$, are obtained by applying to the extrinsic curvature K_{ij} the following conformal transformations and decompositions:

$$K_{ij} = A_{ij} + \frac{1}{3}\gamma_{ij} K \quad (9)$$
$$A_{ij} = \Phi^{-2} \bar A_{ij} \quad (10)$$
$$\bar A_{ij} = \bar A^{\rm TT}_{ij} + (\bar L \mathcal{W})^{ij}\,, \quad (11)$$

with $K \equiv K^i{}_i$, $(\bar L\mathcal{W})^{ij} \equiv \bar\nabla^i \mathcal{W}^j + \bar\nabla^j \mathcal{W}^i - \frac{2}{3}\bar\gamma^{ij}\bar\nabla_k \mathcal{W}^k$ and $\bar\nabla_i \bar A^{ij}_{\rm TT} = 0$. The operator $\bar\nabla$ denotes covariant differentiation associated with the confomal spatial metric $\bar\gamma_{ij}$. Notice that A_{ij} and $\bar A_{ij}$ are traceless, and $\bar A^{\rm TT}_{ij}$ is transverse. With these transformations, Eqs. (1) and (2) reduce to

$$\begin{aligned} 8\bar\Delta\Phi - \Phi\,\bar R - \frac{2}{3}\Phi^5 K^2 &+ \Phi^{-7}\bar A_{ij}\bar A^{ij} \\ &= -16\,\pi\Phi^5\,\rho_{\rm H} \end{aligned} \quad (12)$$
$$(\bar\Delta_{\rm L}\mathcal{W})^i - \frac{2}{3}\Phi^6\,\bar\nabla^i K = 8\,\pi\,\Phi^{10} S^i \quad (13)$$

respectively, with $(\bar\Delta_L \mathcal{W})^i \equiv \bar\nabla_j (\bar L\mathcal{W})^{ij}$, $\bar\Delta \equiv \bar\nabla_i\bar\nabla^i$, and $\bar R$ the Ricci scalar of the conformal space.

Given Eqs. (12) and (13), constructing initial data translates into freely specifying the quantities $\{\bar\gamma_{ij}, K, \bar A^{\rm TT}_{ij}, \rho_{\rm H}, S^i\}$, and solving for the conformal factor Φ and vector the $\mathcal{W}^i$. A common choice, which we adopt, is to assume conformal flatness ($\bar\gamma_{ij} = \eta_{ij}$), maximal slicing ($K = 0$), and $\bar A^{\rm TT}_{ij} = 0$. Under these assumptions, the constraints (12) and (13) assume the form

$$\bar\Delta\Phi + \frac{1}{8}\Phi^{-7}\bar A_{ij}\bar A^{ij} = -2\,\pi\Phi^5\,\rho_{\rm H} \quad (14)$$
$$(\bar\Delta_L\mathcal{W})^i = 8\,\pi\,\Phi^{10} S^i \quad (15)$$

with $\bar A^{ij} = (\bar L\mathcal{W})^{ij}$. We exploit the freedom to conformally transform $\rho_{\rm H}$ and S^i and set

$$\bar\rho_{\rm H} = \rho_{\rm H}\,\Phi^8\,, \quad (16)$$
$$\bar S^i = S^i\,\Phi^{10}\,, \quad (17)$$

and thus Eqs. (14) and (15) read

$$\bar{\Delta}\Phi + \frac{1}{8}\Phi^{-7}\bar{A}_{ij}\bar{A}^{ij} = -2\,\pi\Phi^{-3}\,\bar{\rho}_{\rm H} \tag{18}$$

$$(\bar{\Delta}_L\mathcal{W})^i = 8\,\pi\,\bar{S}^i\,. \tag{19}$$

The transformations (16) and (17), and the expressions (6) and (7) suggest setting in the stress-energy tensor $\bar{\rho} = \Phi^8\rho$, $\bar{p} = \Phi^8\,p$ and $\bar{u}^i = \Phi^2 u^i$, and therefore

$$\bar{\rho}_{\rm H} = (\bar{\rho}+\bar{p})\,W^2 - \bar{p}\,, \tag{20}$$

$$\bar{S}^i = (\bar{\rho}+\bar{p})W\,\bar{u}^i\,, \tag{21}$$

Notice from $u^a u_a = -1$ that $W^2 - 1 = \gamma_{ij}u^i u^j = \bar{\gamma}_{ij}\bar{u}^i\bar{u}^j = \bar{W}^2 - 1$. Then, with the help of Eq. (21),

$$W^2 - 1 = \bar{\gamma}_{ij}\bar{u}^i\bar{u}^j = \frac{\bar{S}^2}{W^2(\bar{\rho}+\bar{p})^2}\,, \tag{22}$$

and thus

$$W^2 = \frac{1}{2}\left(1 + \sqrt{1 + \frac{4\,\bar{S}^2}{(\bar{\rho}+\bar{p})^2}}\right)\,, \tag{23}$$

where $\bar{S}^2 = \bar{\gamma}_{ij}\bar{S}^i\bar{S}^j$.

In summary, constructing initial data reduces to first specifying $\bar{\rho}_{\rm H}$ and $\bar{S}^i$, next solving Eq. (19) for $\mathcal{W}^i$ to construct $\bar{A}^{ij}$, and finally solving for Φ from Eq. (18).

III. EXTRINSIC CURVATURE

We now consider solutions to the momentum constraint equation $(\bar{\Delta}_L\mathcal{W})^i = 8\,\pi\,\bar{S}^i$. We will first recall the solution that represents BHs and next reintroduce the one suitable to model NSs. For BHs ($\bar{S}^i = 0$), Bowen and York [25] found that point-source solutions to $(\bar{\Delta}_L\mathcal{W})^i = 0$ are given by

$$\mathcal{W}^i = -\frac{1}{4\,r}\left[7\,P^i + l^i(P\cdot l)\right] \tag{24}$$

$$\mathcal{W}^i = \frac{1}{r^2}\epsilon^{ijk}l_j J_k\,, \tag{25}$$

with $l^i = x^i/r$ a unit radial vector and $P\cdot l = P^i l_i$. In these solutions, the constant vectors P^i and J_i are respectively interpreted as the linear and angular momentum of the BH. From $\bar{A}^{ij} = (\bar{L}\mathcal{W})^{ij}$, the extrinsic curvature associated with these solutions are:

$$\bar{A}^{ij} = \frac{3}{2\,r^2}\left[P^i l^j + P^j l^i - (\eta^{ij} - l^i l^j)(P\cdot l)\right] \tag{26}$$

$$\bar{A}^{ij} = \frac{6}{r^3}l^{(i}\epsilon^{j)kl}J_k l_l \tag{27}$$

Next is to consider solutions to $(\bar{\Delta}_L\mathcal{W})^i = 8\,\pi\,\bar{S}^i$ that can be used to build the extrinsic curvature of a NS. Following Bowen [40], we assume sources of the form

$$\bar{S}^i = P^i\,\sigma(r) \tag{28}$$

$$\bar{S}_i = \epsilon_{ijk}\,J^j x^k\,\kappa(r)\,. \tag{29}$$

At this point, P^i and J^i arbitrary constant vectors, and σ and κ radial functions with compact support on $r \le r_0$. The specific form of these functions will be determined in the next section using the following conditions.

From the definition of ADM linear momentum [41], one has that

$$\begin{aligned} P^i_{\rm ADM} &= \frac{1}{8\pi}\int_{\partial\Sigma_\infty} A^{ij}\,dS_j \\ &= \frac{1}{8\pi}\int_\Sigma \bar{\nabla}_j\bar{A}^{ij}\sqrt{\eta}\,d^3x \\ &= \int_\Sigma \bar{S}^i\sqrt{\eta}\,d^3x \\ &= P^i\int_\Sigma \sigma\sqrt{\eta}\,d^3x\,. \end{aligned} \tag{30}$$

Thus, for $P^i_{\rm ADM} = P^i$ to hold, σ must satisfy the following normalization condition:

$$\int_\Sigma \sigma\sqrt{\eta}\,d^3x = 4\,\pi\int_0^{r_0}\sigma\,r^2\,dr = 1\,. \tag{31}$$

Similarly, from the definition of ADM angular momentum [12], we have that

$$\begin{aligned} J^{\rm ADM}_i &= \frac{1}{8\pi}\epsilon_{ijk}\int_{\partial\Sigma_\infty} x^j A^{km}\,dS_m \\ &= \frac{1}{8\pi}\epsilon_{ijk}\int_\Sigma x^j\bar{\nabla}_m\bar{A}^{km}\sqrt{\eta}\,d^3x \\ &= \epsilon_{ijk}\int_\Sigma x^j\,\bar{S}^k\sqrt{\eta}\,d^3x \\ &= \epsilon_{ijk}\epsilon^{klm}\int_\Sigma x^j J_l x_m\,\kappa\sqrt{\eta}\,d^3x \\ &= \int_\Sigma r^2\left(J_i - l_i l^j J_j\right)\kappa\sqrt{\eta}\,d^3x\,. \end{aligned} \tag{32}$$

Adopting Cartesian coordinates and aligning the angular momentum with the z-axis, one gets that

$$J^{\rm ADM}_i = J_i\int_\Sigma r^2\,\sin^2\theta\,\kappa\sqrt{\eta}\,d^3x\,. \tag{33}$$

Thus, in order to have $J^{\rm ADM}_i = J_i$, the following normalization condition must hold

$$2\,\pi\int_0^{r_0}\int_0^\pi \sin^3\theta\,r^4\kappa\,d\theta\,dr = \frac{8\,\pi}{3}\int_0^{r_0}\kappa\,r^4\,dr = 1\,. \tag{34}$$

Given the normalization condition Eq. (31) for σ, the solution to $(\bar{\Delta}_L\mathcal{W})^i = 8\,\pi\,P^i\,\sigma$ reads [40]

$$\mathcal{W}^i = -2\,P^i F + \frac{1}{2}P^i H + \frac{1}{2}l^i(P\cdot l)\,rH'\,, \tag{35}$$

where primes denote differentiation with respect to the radial coordinate r. The functions F and H are given respectively by

$$F = \frac{1}{r}\int_0^r 4\,\pi\,\sigma\,\tilde{r}^2\,d\tilde{r} + \int_r^{r_0} 4\,\pi\,\sigma\,\tilde{r}\,d\tilde{r}\,, \tag{36}$$

$$H = \frac{1}{r^3}\int_0^r F\,\tilde{r}^2\,d\tilde{r}\,. \tag{37}$$

With the help of $\bar{\nabla}^i r = l^i$ and $\bar{\nabla}^i l^j = (\eta^{ij} - l^i l^j)/r$, substitution of Eq. (35) into $\bar{A}^{ij} = (\bar{L}\mathcal{W})^{ij}$ yields

$$\begin{aligned}\bar{A}^{ij} &= (-2\,F' + H')(P^i l^j + P^j l^i) \\ &+ (rH'' - H')(P\cdot l) l^i l^j \\ &+ \frac{1}{3}(4\,F' - rH'' - H')(P\cdot l)\eta^{ij}\,. \end{aligned} \tag{38}$$

With the help of

$$Q = \int_0^r 4\pi\sigma\tilde{r}^2\,d\tilde{r} \tag{39}$$

$$J = \int_r^{r_0} 4\pi\sigma\tilde{r}\,d\tilde{r} \tag{40}$$

$$\begin{aligned} C &= \int_0^r \frac{2}{3}\pi\sigma\tilde{r}^4\,d\tilde{r} \\ &= \int_0^r \left(\frac{1}{2}Q\tilde{r}^2 + \frac{1}{3}J\tilde{r}^3\right) d\tilde{r}\,, \end{aligned} \tag{41}$$

and

$$F = Q/r + J \tag{42}$$

$$H = Q/2r + J/3 - C/r^3 \tag{43}$$

$$F' = -Q/r^2 \tag{44}$$

$$H' = -Q/2r^2 + 3C/r^4 \tag{45}$$

$$H'' = Q/r^3 - 12C/r^5\,, \tag{46}$$

the expression (38) for the extrinsic curvature can be rewritten as

$$\begin{aligned}\bar{A}^{ij} &= \frac{3Q}{2\,r^2}\left[P^i l^j + P^j l^i - (\eta^{ij} - l^i l^j)(P\cdot l)\right] \\ &+ \frac{3C}{r^4}\left[P^i l^j + P^j l^i + (\eta^{ij} - 5\,l^i l^j)(P\cdot l)\right]\,. \end{aligned} \tag{47}$$

For $r > r_0$ (exterior solution), $Q = 1$, thus the first term in Eq. (47) becomes the Bowen-York curvature for a point mass (26). Furthermore, Eq. (47) has the correct point mass limit since $Q = 1$ and $C = 0$ for $r_0 = 0$.

For a spherically symmetric source function κ with angular momentum J^i, the solution to $(\bar{\Delta}_L\mathcal{W})_i = 8\,\pi\,\epsilon_{ijk}J^j x^k\,\kappa$ is given by [42]

$$\mathcal{W}_i = \epsilon_{ijk}\,x^j J^k\,G \tag{48}$$

where

$$G = \frac{1}{r^3}\int_0^r \frac{8\,\pi}{3}\,r'^4\,\kappa\,dr' + \int_r^{r_0}\frac{8\,\pi}{3}\kappa\,r'\,dr'\,. \tag{49}$$

Notice that $G = r^{-3}$ for $r \geq r_0$. Substitution of Eq. (48) into $\bar{A}^{ij} = (\bar{L}\mathcal{W})^{ij}$ yields

$$\bar{A}^{ij} = \frac{6}{r^3}l^{(i}\epsilon^{j)kl}J_k l_l N \tag{50}$$

where

$$N = \int_0^r \frac{8\,\pi}{3}\,r'^4\,\kappa\,dr' \tag{51}$$

Exterior to the source, $N = 1$, and the extrinsic curvature reduces to the point-like solution (27).

In summary, Eqs. (26) and (27) are the extrinsic curvatures for a point-like source with linear and angular momentum, respectively. In addition, Eqs. (47) and (50) are the extrinsic curvatures for a spherically symmetric source with linear and angular momentum, respectively. To construct initial data for compact object binaries, the extrinsic curvature for the binary system will be simply given by a superposition of these solutions, point-like for the BH and spherically symmetric source for the NS. The only input needed are the locations of the compact objects, their linear and angular momenta, and the source functions σ and κ. As with BBHs, the linear and angular momenta of the sources, and their binary separation will be provided by the outcome of integrating the PN equations of motion. It is very important to keep in mind that, because of the spherical symmetry assumption in the source functions σ and κ, the extrinsic curvature will not be able to account for tidal deformations of the star. We are currently considering a generalization that relaxes the spherical symmetry assumption.

IV. SOURCE FUNCTIONS

The next step is to specify the source functions σ and κ, as well as the source $\bar{\rho}_{\rm H} = (\bar{\rho} + \bar{p})\,W^2 - \bar{p}$ in the Hamiltonian constraint. The starting point is the density $\bar{\rho}$ and pressure $\bar{p}$ from the stellar model of our choice, Recall from Eq. (4) that $\bar{S}^i = (\bar{\rho} + \bar{p})W\,\bar{u}^i$. Thus, for the case of linear momentum, we have that

$$\bar{S}^i = (\bar{\rho} + \bar{p})W\,\bar{u}^i = P^i\,\sigma\,. \tag{52}$$

We then set

$$\sigma = (\bar{\rho} + \bar{p})/\mathcal{M}\,, \tag{53}$$

with $\mathcal{M}$ a constant determined by the normalization condition Eq. (31) for σ. That is,

$$1 = 4\,\pi\int_0^{r_0}\sigma\,r^2\,dr = \frac{4\,\pi}{\mathcal{M}}\int_0^{r_0}(\bar{\rho} + \bar{p})\,r^2\,dr\,, \tag{54}$$

and thus

$$\mathcal{M} = 4\,\pi\int_0^{r_0}(\bar{\rho} + \bar{p})\,r^2\,dr\,, \tag{55}$$

Notice that Eq. (53) restricts our choice for $\bar{\rho}$ and $\bar{p}$ to be spherically symmetry solutions since by assumption $\sigma(r)$. With this choice for σ, the linear momentum satisfies $P^i = W\,\mathcal{M}\,\bar{u}^i$. Since by construction P^i and $\mathcal{M}$ are constants, $W\,\bar{u}^i$ must also be constant within the source distribution. Finally, notice also from Eqs. (23), (52) and (53) that the Lorentz factor is then given by

$$W^2 = \frac{1}{2}\left(1 + \sqrt{1 + \frac{4\,P^2}{\mathcal{M}^2}}\right)\,. \tag{56}$$

where $P^2 = \eta_{ij} P^i P^j$.

For a source with angular momentum,

$$\bar{S}_i = \epsilon_{ijk}\, J^j x^k\, \kappa = (\bar{\rho} + \bar{p}) W\, \bar{u}_i\,. \tag{57}$$

As with the previous case, we set

$$\kappa = (\bar{\rho} + \bar{p})/\mathcal{N}\,,\,. \tag{58}$$

From the normalization condition Eq. (34), one has that

$$1 = \frac{8\,\pi}{3} \int_0^{r_0} \kappa\, r^4\, dr = \frac{8\,\pi}{3\,\mathcal{N}} \int_0^{r_0} (\bar{\rho} + \bar{p})\, r^4\, dr\,, \tag{59}$$

and thus the constant $\mathcal{N}$ is given by

$$\mathcal{N} = \frac{8\,\pi}{3} \int_0^{r_0} (\bar{\rho} + \bar{p})\, r^4\, dr\,, \tag{60}$$

The Lorentz factor in this case reads

$$W^2 = \frac{1}{2}\left(1 + \sqrt{1 + \frac{4\,J^2 r^2 \sin^2\theta}{\mathcal{N}^2}}\right)\,. \tag{61}$$

where J is the magnitude of the angular momentum and θ the angle between J^i and l^i. Notice that in this case the Lorentz boost factor is not constant within the star.

An important aspect to keep in mind is how the spin enters for consistency in several ways during the construction of initial data. The spin enters explicitly in the extrinsic curvature tensor and, as a consequence, in the source of the momentum constraint. It is also involved in the normalization condition imposed by the ADM angular momentum. Finally, the spin appears in the source of the Hamiltonian constraint through the Lorentz boost factor.

V. INITIAL DATA PROCEDURE

The centerpiece of our method is solving Eq. (18), or equivalently

$$\bar{\Delta}\Phi + \frac{1}{8}\Phi^{-7} \bar{A}_{ij} \bar{A}^{ij} = -2\,\pi \Phi^{-3} [(\bar{\rho} + \bar{p})\, W^2 - \bar{p}]\,. \tag{62}$$

In this equation, the boost factor W for the stellar model is given by Eq. (56) for linear momentum or Eq. (61) for angular momentum. In the same equation, $\bar{A}^{ij}$ is given by the Bowen-York extrinsic curvatures. For point masses, Eq. (26) provides the extrinsic curvature with linear momentum and Eq. (27) the corresponding extrinsic curvature with angular momentum. Similarly, the extrinsic curvature associated with the stellar model is given by Eq. (47) for linear momentum and Eq. (50) for angular momentum.

In general terms, the sequence of steps to construct initial data for binaries with BHs and NSs components under the proposed method is as follows:

1. Choose masses $M_{1,2}$ of the compact objects and their initial separation d_0 deep in the PN regime, with $M = M_1 + M_2$ the total mass of the binary and $q = M_1/M_2$ its mass ratio. Integrate the PN equations of motion at the highest order available and stop at a separation d where the NR evolution will begin. Read off the linear momentum $\vec{P}_{1,2}$ and spin $\vec{S}_{1,2}$ for each of the binary components.

2. Identify the mass $M_{1(2)}$ with the ADM mass $M^{\rm ADM}_{1(2)}$ of a star in isolation if a NS and with the irreducible mass $M^{\rm irr}_{1(2)}$ if a BH, where

$$M_{\rm ADM} = -\frac{1}{2\pi} \int_{\partial\Sigma_\infty} \bar{\nabla}^i \Phi\, dS_i\,, \tag{63}$$

and $M_{\rm irr} \equiv \sqrt{\mathcal{A}/16\,\pi}$ for a BH with apparent horizon area $\mathcal{A}$ [12].

3. If object 1(2) is a BH, set its puncture bare mass $m_{1(2)} = M_{1(2)}$. If object 1(2) is a NS, construct a spherically symmetric stellar model with ADM mass $M^{\rm ADM}_{1(2)}$. Compute also its rest mass $M^0_{1(2)}$ from

$$M_0 = \int_\Sigma \rho_0\, W\, \sqrt{\gamma}\, d^3x\,, \tag{64}$$

and save the ratio $\xi_{1(2)} \equiv M^{\rm ADM}_{1(2)}/M^0_{1(2)}$.

4. If the compact object is a NS, calculate the functions σ and κ from Eqs. (53) and (58), respectively.

5. Use the $\vec{P}$ and $\vec{S}$ vectors to construct the extrinsic curvature using Eqs. (26) and (27) if a BH, and Eqs. (47) and (50) if a NS. The functions σ and κ will also be needed if a NS. The total extrinsic curvature is $\bar{A}^{ij} = \bar{A}^{ij}_1 + \bar{A}^{ij}_2$.

6. Construct the term $[(\bar{\rho} + \bar{p})\, W^2 - \bar{p}]$ in the r.h.s. of Eq. (62) for each NS. Superpose the terms if the binary involves a DNS.

7. Solve the Hamiltonian constraint in the form given by Eq. (62).

8. If a BH, compute the new irreducible $\hat{M}^{\rm irr}_{1(2)}$, and if a NS calculate the new rest mass $\hat{M}^0_{1(2)}$. Using $\xi_{1(2)}$ from Step 3, estimate the new ADM mass $\hat{M}^{\rm ADM}_{1(2)} = \xi_{1(2)} \hat{M}^0_{1(2)}$. Notice that we are assuming that the ratio $\xi_{1(2)}$ does not change significantly from iteration to iteration.

9. Next, identify the new mass $\hat{M}_{1(2)}$ with $\hat{M}^{\rm ADM}_{1(2)}$ if a NS and $\hat{M}_{1(2)}$ with $\hat{M}^{\rm irr}_{1(2)}$ if a BH. Calculate the new total mass $\hat{M} = \hat{M}_1 + \hat{M}_2$ and mass ratio $\hat{q} = \hat{M}_1/\hat{M}_2$. If the new values differ from the values in Step 1 by more than a specified tolerance, adjust the bare masses of the BH or central densities of the NS according to a 2D secant algorithm [43], and return to step 3.

For the present work, we solve Eq. (62) using a modified version of the 2Punctures spectral code. 2Punctures was originally developed by Ansorg [7] to construct BBH initial data; that is, to solve Eq. (62) with vanishing r.h.s. and A_{ij} given by Eqs. (26) and/or (27).

Once the conformal factor Φ is found from solving Eq. (62), the spatial metric and extrinsic curvature are obtained from $\gamma_{ij} = \Phi^4 \eta_{ij}$ and $K_{ij} = \Phi^{-2} \bar{A}_{ij}$, respectively. The last step is constructing the hydrodynamical fields ρ, p, W and u^i. Given Φ, $\bar{\rho}_H$ and $\bar{S}^i$, we have that ρ_H and S^i are considered as known since $\rho_{\rm H} = \Phi^{-8} \bar{\rho}_H$ and $S^i = \Phi^{-10} \bar{S}^i$. On the other hand,

$$\rho_{\rm H} = (\rho + p)\, W^2 - p \tag{65}$$
$$S^i = (\rho + p) W u^i \,, \tag{66}$$

and from the second equation,

$$\begin{aligned} \gamma_{ij} S^i S^j &= (\rho + p)^2 W^2 \gamma_{ij} u^i u^j \\ &= (\rho + p)^2 W^2 (W^2 - 1) \,, \end{aligned} \tag{67}$$

where in the last equality we used that $\gamma_{ij} u^i u^j = W^2 - 1$ as implied by $u^a u_a = -1$. If we view that p is given by an equation of state, Eqs. (65) and (67) can be used to solve for ρ and W. And the last step is to construct u^i from Eq. (66).

VI. TOLMAN-OPPENHEIMER-VOLKOFF MODEL IN ISOTROPIC COORDINATES

For the present work, we use a Tolman-Oppenheimer-Volkoff (TOV) stellar model to represent a NS, with a polytropic equation of state $p = K \rho_0^\Gamma$. Since we assume conformal flatness, it is natural to recast the TOV model in isotropic coordinates. TOV models are commonly constructed in coordinates in which the metric takes the form

$$ds^2 = -\alpha^2(\hat{r})\, dt^2 + \left[1 - \frac{2\, m(\hat{r})}{\hat{r}}\right]^{-1} d\hat{r}^2 + \hat{r}^2\, d\Omega \,. \tag{68}$$

On the other hand, the form of the metric (isotropic) compatible with our conformal flatness assumption is

$$ds^2 = -\alpha^2(r)\, dt^2 + \Phi(r)^4 (dr^2 + r^2\, d\Omega) \,. \tag{69}$$

In these coordinates, the equations that one needs to solve are the so called "conformal thin sandwich" equations [12].

$$\partial^i \partial_i \Phi = -\frac{1}{8} \Phi^{-7} \bar{A}_{ij} \bar{A}^{ij} - 2\,\pi \Phi^5\, \rho_H \tag{70}$$

$$\partial^j \partial_j \beta^i + \frac{1}{3} \partial^i \partial_j \beta^j = 2\, \bar{A}^{ij} \partial_j (\alpha\, \Phi^{-6}) + 16\, \pi\, \alpha\, \Phi^4\, S^i \tag{71}$$

$$\partial^i \partial_i (\alpha\, \Phi) = \alpha\, \Phi \left[\frac{7}{8} \Phi^{-8} \bar{A}_{ij} \bar{A}^{ij} + 2\,\pi \Phi^4 (\rho_H + 2\, S)\right] \tag{72}$$

where β^i is the shift vector, ρ_H is given by Eq. (6), S^i by Eq. (7) and $S = S^i{}_i$ with $S_{ij} = \gamma_i^a \gamma_j^b T_{ab}$.

For the metric (69), the conformal thin sandwich equations reduce to

$$\frac{1}{r^2} (r^2\, \Phi')' = -2\,\pi \Phi^5\, \rho \tag{73}$$

$$\frac{1}{r^2} (r^2\, \Theta')' = 2\,\pi\, \Theta \Phi^4 (\rho + 6\, p) \tag{74}$$

where primes denote differentiation with respect to r and $\Theta \equiv \alpha\, \Phi$. Notice also that in this case $\beta^i = 0$, $A^{ij} = 0$, $S^i = 0$ and $\rho_H = \rho$. Finally, from $\nabla_b T^{ab} = 0$, one obtains

$$p' = -(\rho + p) \frac{\alpha'}{\alpha} = -(\rho + p) \left(\frac{\Theta'}{\Theta} - \frac{\Phi'}{\Phi}\right) \tag{75}$$

Therefore, together with an equation of state, constructing TOV stellar models in isotropic coordinates involves solving Eqs. (73), (74) and (75). Integration constants are chosen such that in the exterior of the star

$$\Phi = 1 + \frac{M}{2\, r} \tag{76}$$
$$\Theta = 1 - \frac{M}{2\, r} \,, \tag{77}$$

with

$$M = 2\pi \int_0^{r_0} r^2 \Phi^5 \rho\, dr \tag{78}$$

the total mass of the star. Notice that $M = M_{\rm ADM}$ the ADM mass since Eq. (78) can be rewritten as Eq. (63).

If we denote by $\Phi_{\rm tov}$, $\rho_{\rm tov}$ and $p_{\rm tov}$ the TOV solutions in isotropic coordinates, we then set

$$\bar{\rho} = \Phi_{\rm tov}^8 \rho_{\rm tov} \tag{79}$$
$$\bar{p} = \Phi_{\rm tov}^8 p_{\rm tov} \,, \tag{80}$$

and rewrite the Hamiltonian constraint Eq. (62) as

$$\begin{aligned} &\bar{\Delta} \Phi + \frac{1}{8} \Phi^{-7} \bar{A}_{ij} \bar{A}^{ij} = \\ &-2\,\pi \Phi^{-3}\, \Phi_{\rm tov}^8 [(\rho_{\rm tov} + p_{\rm tov})\, W^2 - p_{\rm tov}] \end{aligned} \tag{81}$$

Notice that for an isolated TOV stellar model without linear or angular momentum ($\bar{A}_{ij} = 0$, $W = 1$ and $\Phi = \Phi_{\rm tov}$), Eq. (81) reduces to Eq. (73), namely

$$\bar{\Delta} \Phi_{\rm tov} = -2\,\pi \Phi_{\rm tov}^5\, \rho_{\rm tov} \,. \tag{82}$$

VII. SINGLE NEUTRON STAR WITH LINEAR AND ANGULAR MOMENTUM

We test the proposed method in the simple case of an isolated NS. We will first consider a star with linear momentum along the x-axis. As mentioned before, we model the star as a polytrope with equation of state $p = K \rho_0^\Gamma$, setting $\Gamma = 2$ and $K = 123.641\, M_\odot^2$. The star has

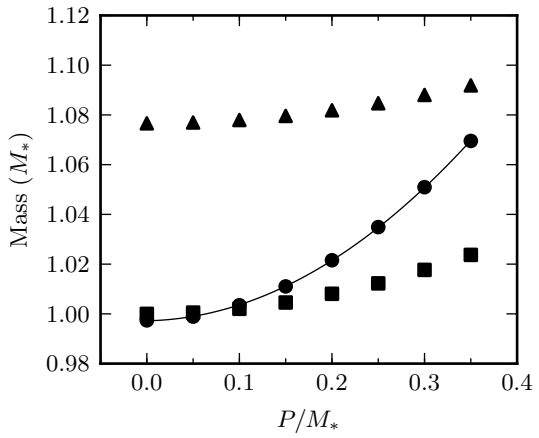

FIG. 1: ADM mass $M_{\rm ADM}$ (dots), rest mass M_0 (triangles) and $M_* W$ (squares) as a function of P/M_* for a single NS. Solid line represents a fit to $M_{\rm ADM} = M_* + cP^2$.

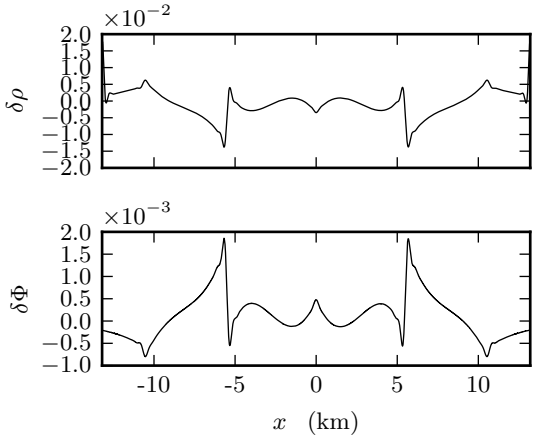

FIG. 2: Relative differences along the x-axis between the TOV solution and the corresponding solution for a TOV star with momentum $P/M_* = 0.1$. Top panel shows the relative differences $\delta\rho$ in total mass-energy and bottom panel those in the conformal factor $\delta\Phi$.

mass $M_* = 1.543\, M_\odot$, radius $R_* = 13.4\,$km, and central density $\rho_c = 6.235 \times 10^{14}{\rm gr\,cm^{-3}}$. We endow the star with linear momentum within the range $0 \leq P/M_* \leq 0.4$.

Figure 1 depicts with dots the ADM mass $M_{\rm ADM}$ as a function of P/M_*, and with triangles the rest mass M_0. In the same figure, squares denote the quantity $M_* W$, where the Lorentz boost factor W is calculated from Eq. (56). Notice that for small values of the linear momentum $M_{\rm ADM} \approx M_* W$. Also, it is not difficult to show from Eq. (63) and the Hamiltonian constraint (81) that $M_{\rm ADM} = M_* + O(P^2)$, consistent with the growth observed in Fig. 1.

To further understand the changes that the momentum introduces to the TOV solution, we plot in Fig. 2 the relative differences with respect to the TOV solution of the total mass-energy density ρ (top panel) and conformal factor Φ (bottom panel) along the x-axis, after solving the Hamiltonian constraint for a star with a linear momentum $P/M_* = 0.1$. The relative differences are computed as follows:

$$\delta\rho \;=\; \frac{\rho - \rho_{\rm tov}}{\rho_{\rm tov}} \tag{83}$$

$$\delta\Phi \;=\; \frac{\Phi - \Phi_{\rm tov}}{\Phi_{\rm tov}} \tag{84}$$

The differences in the mass-energy density are entirely due to the conformal factor. From $\rho = \Phi^{-8}\,\bar{\rho}$ and $\bar{\rho} = \Phi^8_{\rm tov}\,\rho_{\rm tov}$, one has that $\rho = (\Phi/\Phi_{\rm tov})^{-8}\rho_{\rm tov}$, and thus from (83) $\delta\rho = (\Phi^{-8} - \Phi^{-8}_{\rm tov})/\Phi^{-8}_{\rm tov}$.

In general terms, the evolutions of the initial data for a single neutron star with linear momentum were satisfactory. The evolutions were carried out with the same gauge conditions used for puncture BH evolutions [33, 34]. We noticed, however, few percent variations in the size and internal structure in the star during the course of the evolution. The changes in the size of

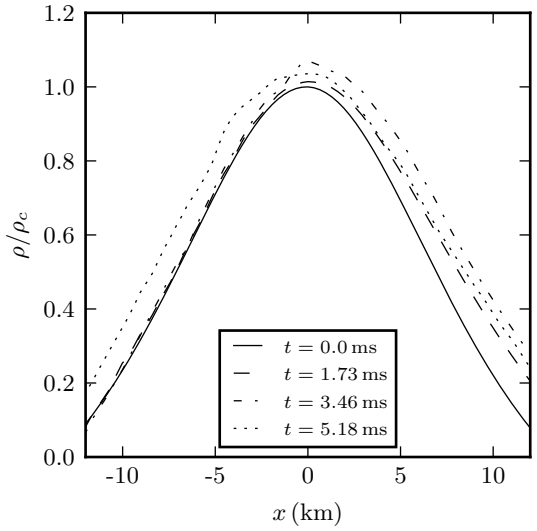

FIG. 3: Density ρ profiles along the x-axis for a TOV star with $P/M_* = 0.1$ at various times throughout the evolution. The profiles have been normalized to the initial central density ρ_c and shifted to be centered at $x = 0$.

the star with linear momentum $\vec{P}/M_* = 0.1\,\hat{x}$ are shown in Fig. 3 along the x-axis and in Fig. 4 along the y-axis. Notice that the deformations are more prominent in the leading edge of the star (i.e. positive x-axis). Oscillations reveal themselves also in the central density of the star. Fig. 5 shows the evolution of the central density in the star for the same case.

Next, we consider a single star with angular momentum. The TOV model for the star is as in the previous case (i.e. polytrope with equation of state $p = K\,\rho_0^\Gamma$,

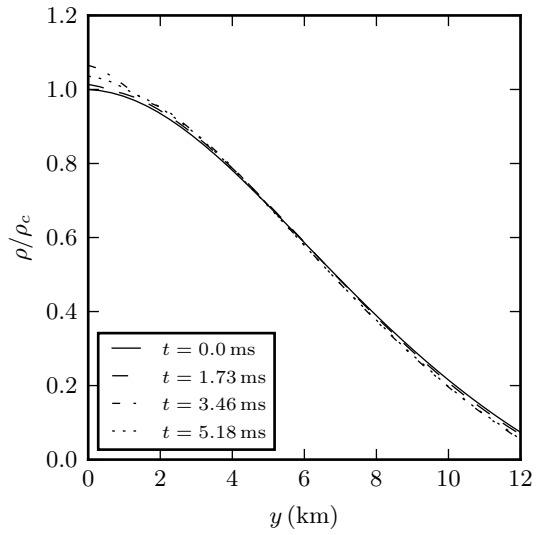

FIG. 4: Density ρ profiles for the same case as in Fig. 3 but along the y-direction. Becuase of reflection symmetry, only half of the profile is shown. The profiles have been normalized to the initial central density ρ_c and intersect with the point of maximum density along the x-axis at all times.

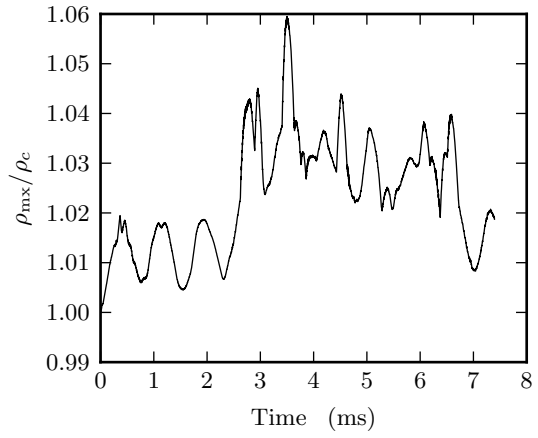

FIG. 5: Evolution of the central density of the star in Fig. 3 normalized to the initial central value ρ_c.

$\Gamma = 2$, $K = 123.641\, M_\odot^2$, mass $M_* = 1.543\, M_\odot$, radius $R_* = 13.4\,$km, and central density $\rho_c = 6.235 \times 10^{14}\mathrm{gr\,cm^{-3}}$). Figure 6 shows the evolution of the central density, normalized to the initial central value ρ_c, for $J/M_*^2 = 0$, 0.025, 0.05, and 0.075, with the angular momentum along the z-axis. Notice the presence of oscillations for all cases, including the non-spinning case. The amplitude of the oscillations increases with the magnitude of the spin, but the frequency seems to remain unchanged. Notice also that the frequency of these spurious oscillations is comparable to the one observed case with linear momentum (see Fig. 5). Finally, Figures 8

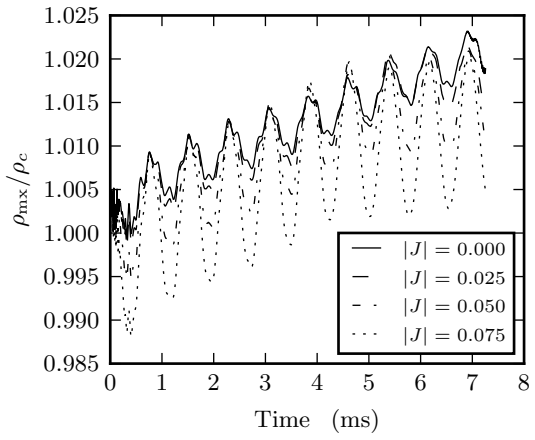

FIG. 6: Evolution of the central density of the spinning star model for J/M_*^2 ranging from 0 to 0.075, with densities normalized to the initial central value ρ_c.

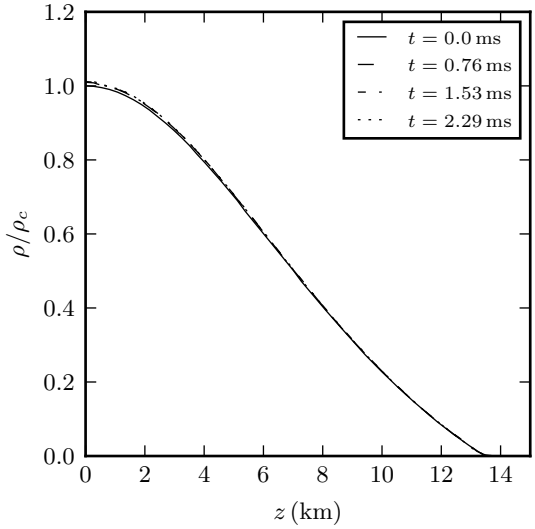

FIG. 7: Density ρ profiles along the z-axis (rotation axis) for a TOV star with $J/M_*^2 = 0.05$ at various times throughout the evolution. The profiles have been normalized to the initial central density ρ_c.

and 7 density ρ profiles along the z-axis (rotation axis) and x-axis, respectively, for a TOV star with angular momentum $J/M_*^2 = 0.05$ at various times throughout the evolution. The profiles have been normalized to the initial central density ρ_c. Notice that changes are more pronounced along the x-axis.

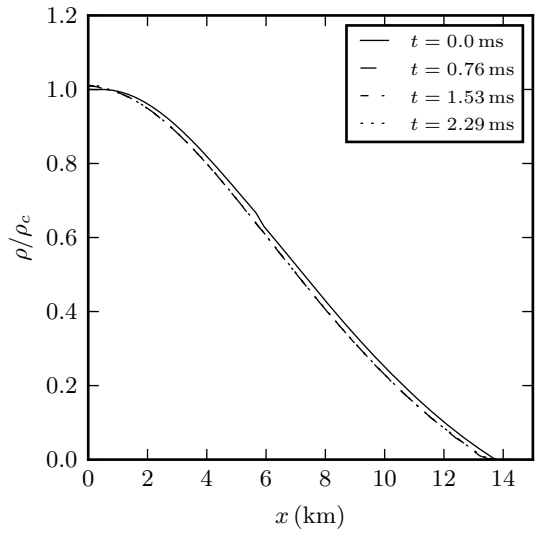

FIG. 8: Density ρ profiles along the x-axis for the TOV star in Fig. 7.

VIII. COMPACT OBJECT BINARY EVOLUTIONS

Next, we test the performance of our prescription to construct initial data with evolutions of DNS and BH-NS binary systems.

A. Non-spinning Double Neutron Star Binary

We consider first an equal-mass DNS system. The NSs have a mass of $1.568\,M_\odot$, coordinate radius 13.1 km, and they are initially separated by 54.6 km. The configuration is similar to the model 1.62-45 in Baiotti et al. [44]. In their case, the stars have a mass of $1.62\,M_\odot$, and their initial coordinate separation is 45 km. The results of this simulation were obtained using 7 levels of mesh refinement. The finest mesh had resolution of $0.150\,M_\odot = 0.221$ km and extent of 26.6 km. The wave-zone grid resolution was $9.58\,M_\odot = 14.1$ km.

Figure 9a shows the coordinate trajectory of one of the NS stars and Fig. 9b the corresponding coordinate separation of the binary. The data in both figures end at the "point-of-contact" (PoC), which occurs at approximately 18 ms after the start of the simulation or at a separation of approximately 25 km. A hypermassive neutron star (HMNS) forms 4 ms after the PoC, which collapses to a BH in approximately 8 ms. The collapse of the HMNS in Baiotti et al. [44] is 10 ms, a difference that we attribute primarily to resolution effects.

Figure 9c shows the evolution of the central density normalized to its initial value. For comparison, see Fig. 12 in Baiotti et al. [44]. The oscillations in Fig. 9c for times earlier than 18 ms are similar, and likely due to the same reasons, to those seen in the case of a single NS with linear momentum (see Fig. 5). Since the amplitude of the oscillations decrease by increasing the initial separation of the binary, we suspect that the origin of the oscillations is because the TOV star has not been able to adjust to the linear momentum added and to the gravitational field by its companion. Similar oscillations have been observed in other initial data methods, for instance, in the work by Tsatsin and Marronetti [19]. To mitigate the oscillations, instead of using a straightforward superposition of the matter sources of each star, Tsatsin and Marronetti [19] apply a weighted average of hydrodynamical fields (see Eq. 9 in [19]), where the weights are functions of the lapse of individual stars. We are currently investigating whether this superposition prescription will also work in our case.

Figure 9d shows the 2,2 mode of the Weyl scalar Ψ_4, extracted at $462\,M_\odot$ from the binary, as a function of retarded time. At the beginning of the waveform, there is a small burst. This is the characteristic unphysical burst of radiation observed in NR simulations that start with conformally flat initial data. After the burst, Ψ_4 shows the expected chirp-like structure, the ringing of the HMNS during the time interval $18\,\text{ms} \leq t \leq 24\,\text{ms}$, and the quasi-normal-mode (QNM) ring-down of the final BH.

Next, we analyze the convergence properties of the Weyl scalar Ψ_4, focusing only in the time segment before merger. We were unable to get "clean" convergence estimates during the HMNS phase since numerical dissipation due to resolution effects leads to significant differences in the longevity of the resulting HMNS [45]. Figure 10 shows differences of amplitude and phase from three simulations with resolutions in the finest grid of 0.45 km (Low), 0.315 km (Medium), and 0.225 km (High). The red line shows the difference (Medium–Low) and the blue line (High–Medium). Assuming 2^{nd} order convergence, the three resolutions imply that (Medium–Low) $\approx 2.49\times$(High–Medium). The black line in Fig. 10 depicts $2.49\times$(High–Medium) and thus consistency with 2^{nd} order convergence. For reference, the sector of the Maya code handling the geometrical fields is by design 6^{nd} order convergent. The hydrodynamical sector however is at best 3^{rd} order, but near shocks and local extrema can deteriorate to 1^{st} order, as seen in codes similar to ours where convergence order could be as low as 1.8 [46].

Finally, Fig. 11 depicts snapshots of the rest-mass density during the evolution. Panels (a), (b) and (c) show the xy-plane and panel (d) the xz-plane. All densities are in units of $\text{g}\,\text{cm}^{-3}$ and distances in units of $M = 3.14\,M_\odot$

B. Spinning Double Neutron Star Binary

The second example of evolution of initial data with the proposed scheme is again an equal-mass binary but now with spinning NSs. Both stars have identical spins, anti-aligned to the orbital axis. The NSs have a mass

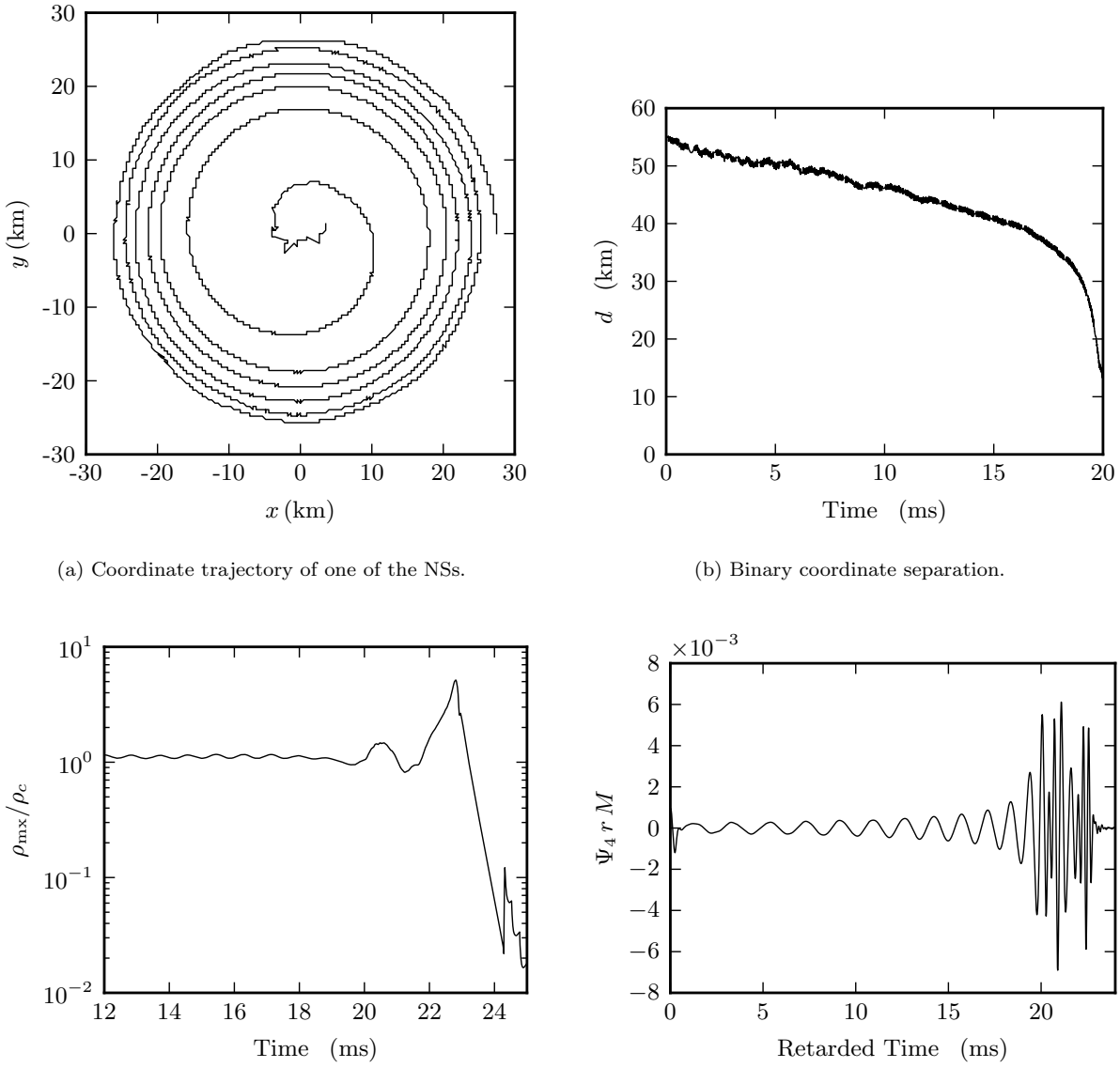

(a) Coordinate trajectory of one of the NSs.

(b) Binary coordinate separation.

(c) Maximum rest mass density normalized to the initial central density ρ_c.

(d) Mode 2,2, of the Weyl scalar Ψ_4.

FIG. 9: Non-spinning NS binary system.

of $1.57\,M_\odot$, coordinate radius 13.1 km, and dimensionless spin parameter $\chi_s = -0.05$. At the beginning of the simulation, the NSs are separated by 61.2 km. With this choice of parameters, the binary system is similar to the case Γ^{--}_{050} in Bernuzzi et al. [47]. The grid structure is as follows: the finest mesh has resolution $0.299M_\odot = .442$ km and extent 26.6 km. The radiation zone has resolution $19.2M_\odot = 28.3$ km.

Figure 12a shows the coordinate trajectory of one of the NS stars and Fig. 12b the corresponding coordinate separation of the binary. Notice from Fig. 12a that the system performs 6 full orbits before merger. Also noticeable is the slight kink or sudden drop in separation observed in Fig. 12b at the beginning of the evolution. After the drop, the inspiral proceeds very smoothly, with minimal spurious eccentricity. As with the previous case, the data in both figures are depicted up to the PoC, which occurs at approximately 25 ms after the start of the simulation or at a separation of 26 km.

Figure 12c shows the evolution of the central density normalized to its initial value. Here again, we observe oscillations in the central density before merger. The HMNS forms at 26.2 ms and lasts for 1.3 ms before it collapses. From the waveform in Fig. 12d, we notice that the HMNS undergoes two bursts. Also, the collapse to BH is faster than in the non-spinning case. This is expected since the spins of NS are anti-aligned with the orbital angular momentum and thus the HMNS is rotat-

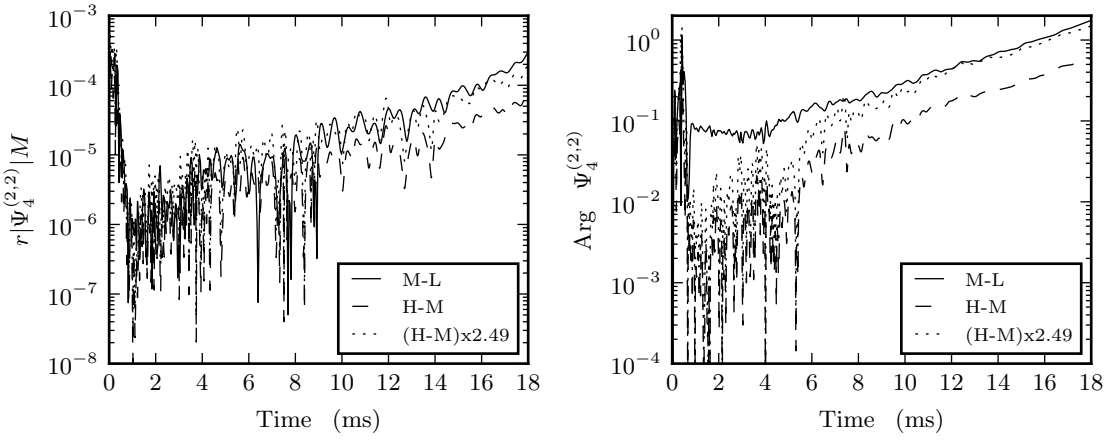

FIG. 10: Amplitude (left panel) and phase (right panel) differences of the Weyl scalar Ψ_4 for three different resolutions of non-spinning DNS system simulations. The resolutions in the finest grid are: 0.45 km (Low), 0.315 km (Medium), and 0.225 km (High). The (Medium–High) resolution is also presented in black re-scaled with a factor of 2.49, corresponding to $2^{\rm nd}$ order convergence.

ing slower than the HMNS in the non-spinning DNS. The energy radiated is estimated to be approximately 0.7% of total mass-energy, and the angular momentum radiated is 16% of total angular momentum. These values are slightly different form those reported by Bernuzzi et al. [47]—which are 1.2% and 18% respectively.

Finally, Fig. 13 depicts snapshots of the rest-mass density during the evolution. Panels (a), (b) and (c) show the xy-plane and panel (d) the xz-plane. All densities are in units of $\mathrm{g\,cm^{-3}}$ and distances in units of $M = 3.14\,M_\odot$.

C. BH-NS Binary

The final example of evolution of initial data is for the case of a BH-NS binary system. The NS has a mass of $1.54 M_\odot$ and a coordinate radius of 13.0 km, and the BH has a mass of $7.7\,M_\odot$ (i.e. 5:1 mass ratio binary). Both compact objects are non-spinning. The coordinate separation between the BH and the NS is 117 km. With these parameters, the BH-NS binary is similar to the M50.145b system in Shibata et al. [48]. As with the DNS system, we cover the star with a single mesh whose side length is the diameter of the star. The grid structure has 8 levels of refinement, with finest resolution of $0.303 M_\odot = 0.448$ km. The finest mesh around the BH has extent $9.10 M_\odot = 13.4$ km. The radiation zone has resolution of $38.8 M_\odot = 57.3$ km.

Figure 14a shows the trajectories of the BH (solid line) and NS (dashed line). The orbital separation of the binary is shown in Fig. 14b. There is clear indication of spurious eccentricity. We attribute this eccentricity to the relatively small initial separation. Figure 14c shows the maximum rest mass density during the course of the evolution. The central density fluctuates as in the previous two cases, with the oscillations decaying at later times. The point at which the central density drops signals the time when the star is disrupted and swallowed by the BH. This is also clear in the 2,2 mode of the Weyl scalar Ψ_4 (see Fig. 14d). At approximately 36 ms, Ψ_4 shows the characteristic QNM ringing of a BH.

Figure 15 depicts snapshots of the rest-mass density during the BH-NS binary evolution. Panels (a), (b) and (c) show the xy-plane and panel (d) the xz-plane. All densities are in units of $\mathrm{g\,cm^{-3}}$ and distances in units of $M = 3.14\,M_\odot$

IX. CONCLUSIONS

We have introduced a new scheme to construct initial data for compact object binaries with NS companions. The method is a generalization of the approach to construct initial data for BBHs in which the BHs are modeled as punctures and the extrinsic curvature is given by the Bowen-York solution to the momentum constraint [25]. In the method introduced in the present work, the extrinsic curvature for the NSs is given by the solution derived by Bowen for spherically symmetric sources with linear momentum [40] and angular momentum [42]. Given these extrinsic curvature solutions, we developed an iterative prescription to construct compact object binary initial data of DNSs or BH-NSs. The prescription has a relatively low computational cost since it only requires solving the Hamiltonian constraint. As with the BBH case, the method also allows one to specify the intrinsic and orbital parameters of the binary with direct input from PN approximations. The quality of the initial data method was demonstrated with a few examples of evolutions: an isolated NS with linear momentum, DNS binaries, including spinning NSs, and a BH-NS system. The evolutions showed general agreement with sim-

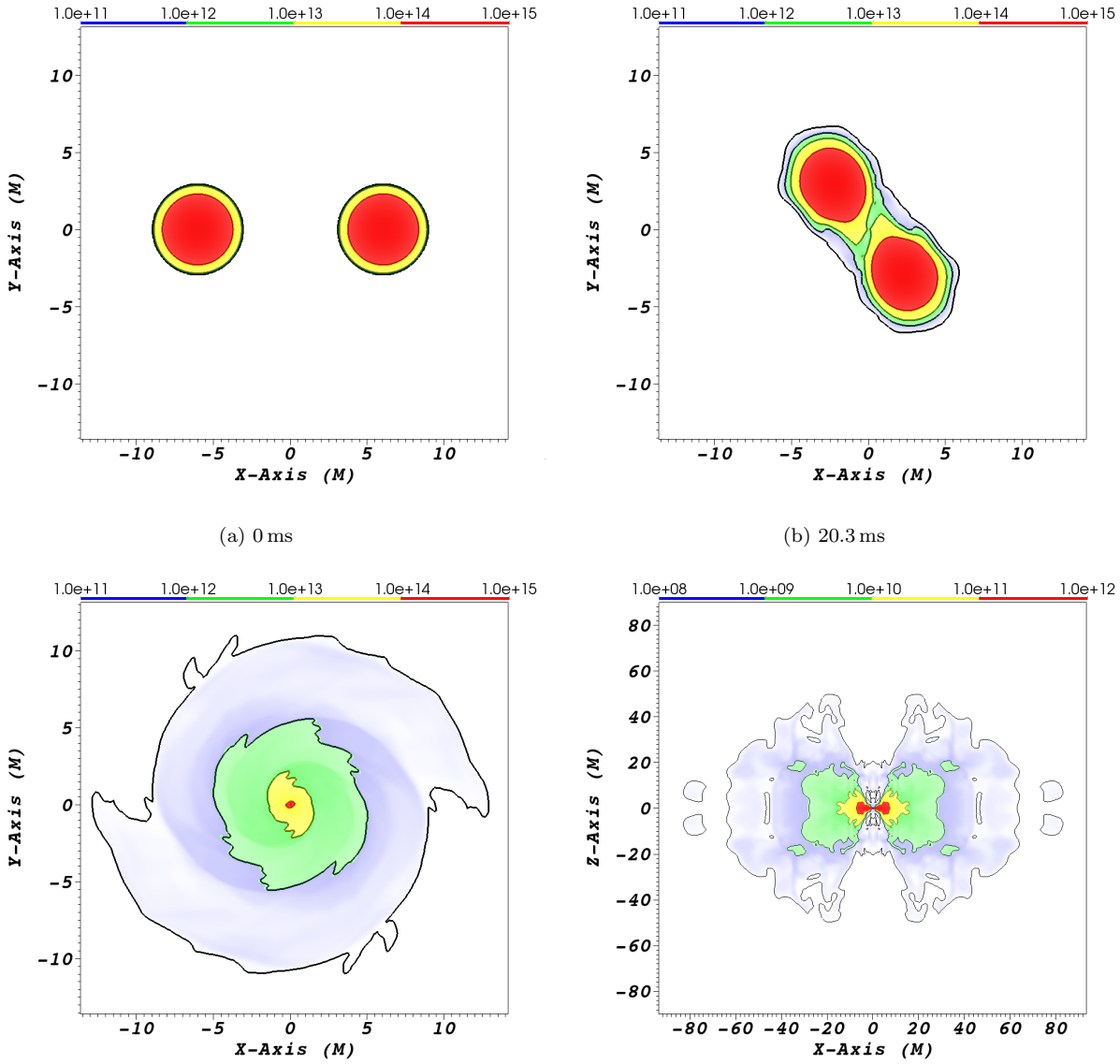

(a) 0 ms

(b) 20.3 ms

(c) 26.9 ms

(d) 24.6 ms

FIG. 11: Rest-mass density snapshots from the non-spinning DNS binary evolution. Panels (a), (b) and (c) show the xy-plane and panel (d) the xz-plane All densities are in units of $\mathrm{g\,cm^{-3}}$ and distances in units of $M = 3.14\,M_\odot$.

ilar cases found in the literature [44, 47, 48].

In this initial incarnation, the method was not devoid of defects. The NSs showed spurious breathing that translated into oscillations in their density structure. We are currently investigating applying the suggestion by Tsatsin and Marronetti [19] to mitigate the oscillations. In addition, for BH-NS binaries and DNS binaries with unequal masses, there is slight drift of the coordinate center-of-mass. In extreme cases, the drift complicates waveform extraction.

Acknowledgments

We thank P. Marronetti for helpful suggestions. This work was supported by NSF grants 1333360 and 1505824. Computations at XSEDE TG-PHY120016 and the Cygnus cluster at Georgia Tech.

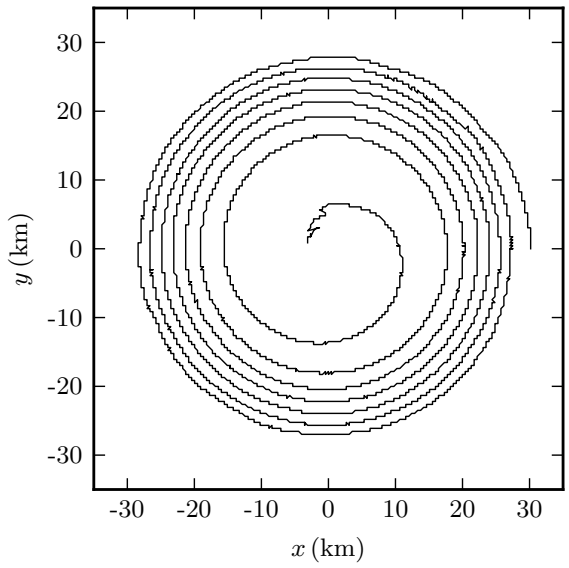

(a) Coordinate trajectory of one of the NS.

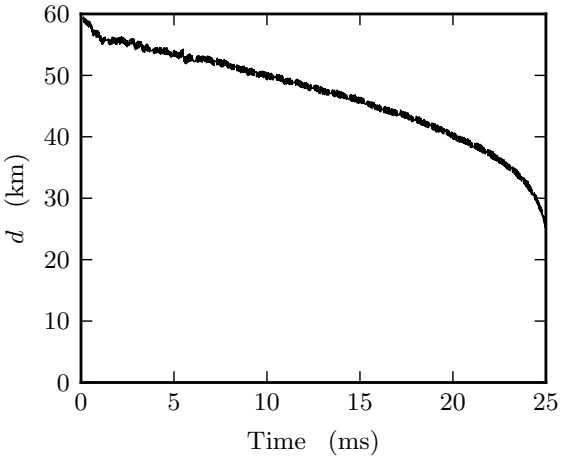

(b) Binary coordinate separation.

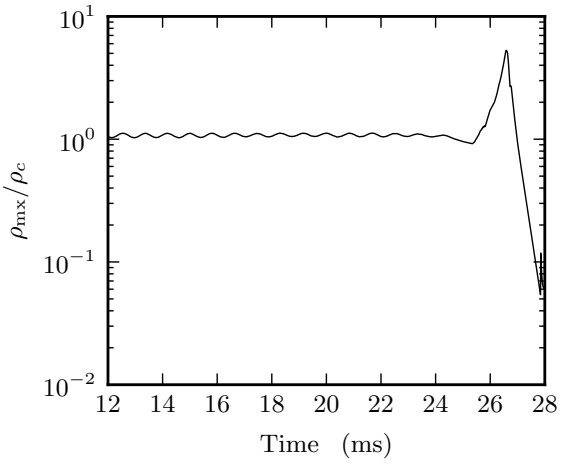

(c) Maximum rest mass density normalized to the initial central density ρ_c.

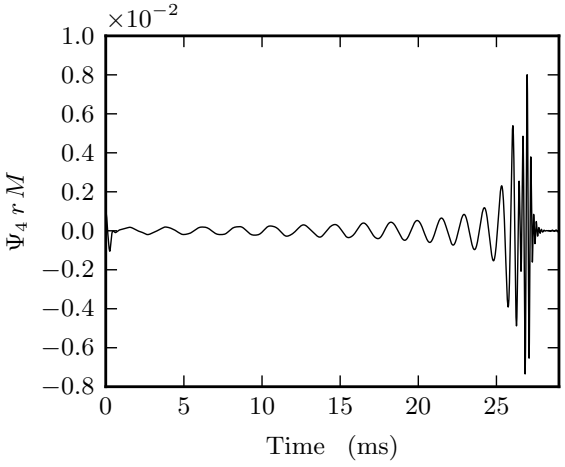

(d) Mode 2,2, of the Weyl scalar Ψ_4.

FIG. 12: Spinning NS binary system

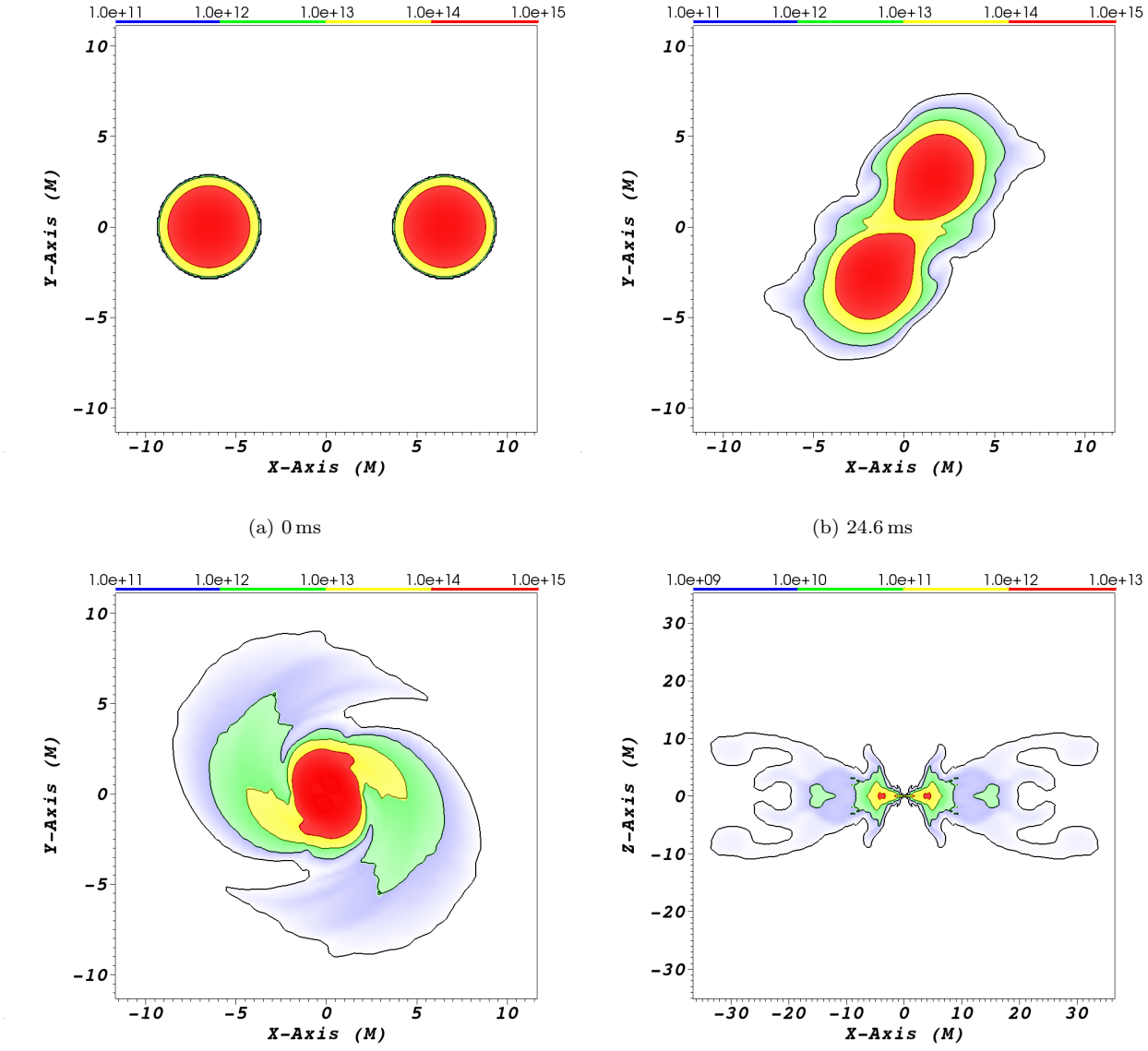

(a) 0 ms

(b) 24.6 ms

(c) 26.1 ms

(d) 29.0 ms

FIG. 13: Rest-mass density snapshots from the spinning DNS binary evolution. Panels (a), (b) and (c) show the xy-plane and panel (d) the xz-plane All densities are in units of $\mathrm{g\,cm^{-3}}$ and distances in units of $M = 3.14\,M_{\odot}$.

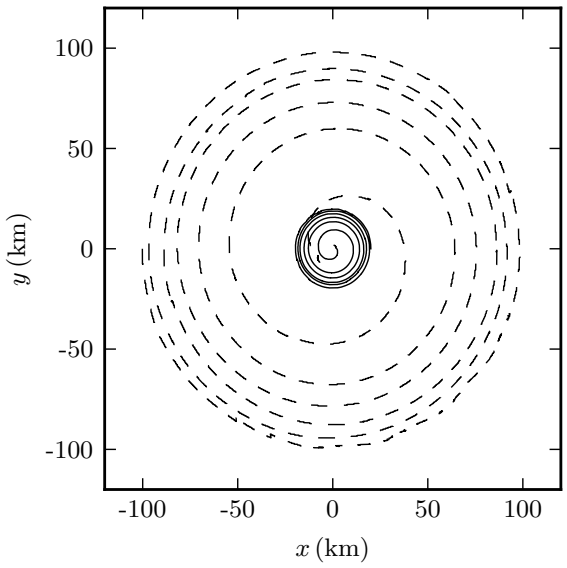

(a) Coordinate trajectories (NS dashed and BH solid)

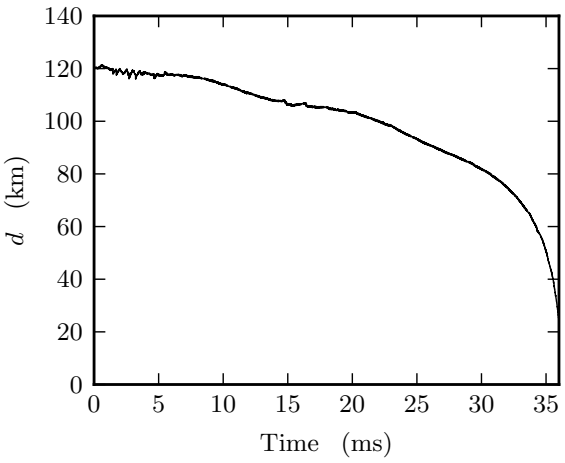

(b) Binary coordinate separation

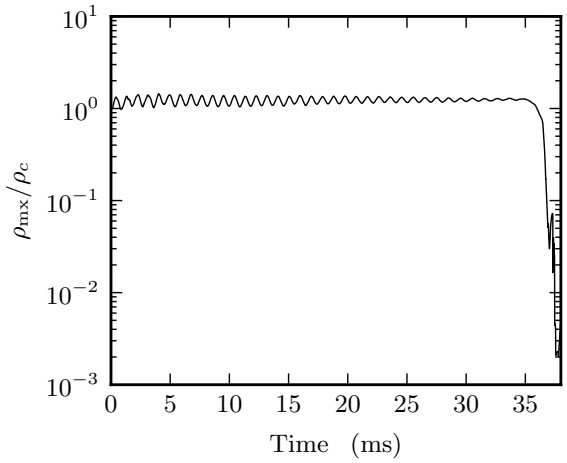

(c) Maximum rest mass density normalized to the initial central density ρ_c.

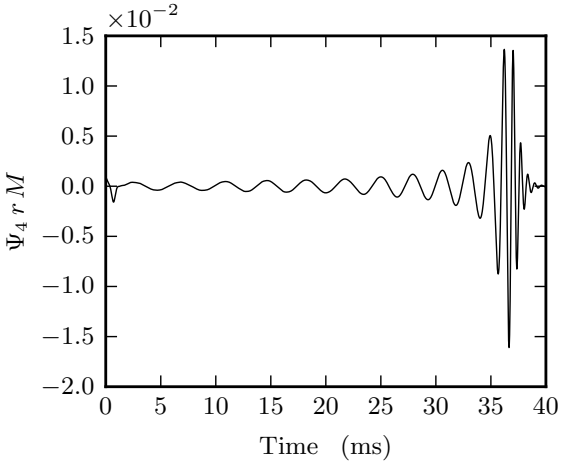

(d) Mode 2,2, of the Weyl scalar Ψ_4.

FIG. 14: BH-NS binary system

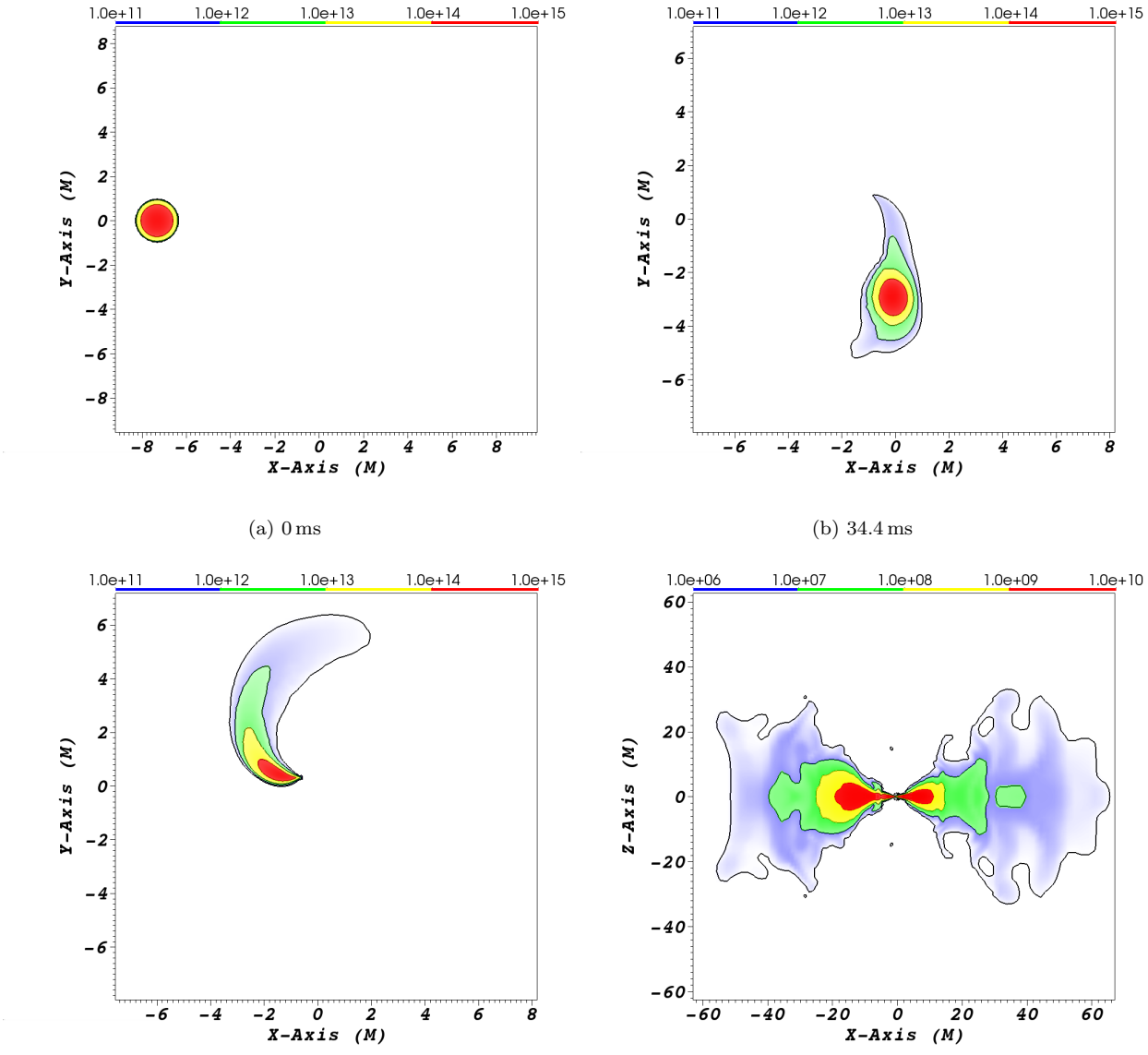

(a) 0 ms

(b) 34.4 ms

(c) 35.9 ms

(d) 37.9 ms

FIG. 15: Rest-mass density snapshots from the bhns binary evolution. Panels (a), (b) and (c) show the xy-plane and panel (d) the xz-plane All densities are in units of $\mathrm{g\,cm^{-3}}$ and distances in units of $M = 3.14\,M_\odot$.

[1] B. P. Abbott, R. Abbott, T. D. Abbott, M. R. Abernathy, F. Acernese, K. Ackley, C. Adams, T. Adams, P. Addesso, R. X. Adhikari, et al., Physical Review Letters **116**, 061102 (2016), 1602.03837.

[2] B. P. Abbott, R. Abbott, T. D. Abbott, M. R. Abernathy, F. Acernese, K. Ackley, C. Adams, T. Adams, P. Addesso, R. X. Adhikari, et al. (LIGO Scientific Collaboration and Virgo Collaboration), Phys. Rev. Lett. **116**, 241103 (2016), URL http://link.aps.org/doi/10.1103/PhysRevLett.116.241103.

[3] The LIGO Scientific Collaboration and the Virgo Collaboration, ArXiv e-prints (2016), 1602.03840.

[4] The LIGO Scientific Collaboration and the Virgo Collaboration, ArXiv e-prints (2016), 1602.03841.

[5] The LIGO Scientific Collaboration and the Virgo Collaboration, ArXiv e-prints (2016), 1602.03843.

[6] S. Brandt and B. Bruegmann, Phys. Rev. Lett. **78**, 3606 (1997), gr-qc/9703066.

[7] M. Ansorg, B. Brügmann, and W. Tichy, Phys. Rev. D **70**, 064011 (2004).

[8] W. Tichy, B. Bruegmann, and P. Laguna, Phys. Rev. **D68**, 064008 (2003), gr-qc/0306020.

[9] P. Grandclément, E. Gourgoulhon, and S. Bonazzola, Phys. Rev. D **65**, 044021 (2002), URL http://link.aps.org/doi/10.1103/PhysRevD.65.044021.

[10] E. Gourgoulhon, P. Grandclément, K. Taniguchi, J.-A. Marck, and S. Bonazzola, Phys. Rev. D **63**, 064029 (2001), gr-qc/0007028.

[11] Z. B. Etienne, J. A. Faber, Y. T. Liu, S. L. Shapiro, K. Taniguchi, and T. W. Baumgarte, Phys. Rev. D **77**, 084002 (2008), URL http://link.aps.org/doi/10.1103/PhysRevD.77.084002.

[12] T. W. Baumgarte and S. L. Shapiro, *Numerical Relativity: Solving Einstein's Equations on the Computer* (Cambridge University Press, 2010).

[13] M. Shibata and K. Taniguchi, Living Reviews in Relativity **14**, 6 (2011).

[14] J. A. Faber and F. A. Rasio, Living Reviews in Relativity **15**, 8 (2012), 1204.3858.

[15] L. Rezzolla, L. Baiotti, B. Giacomazzo, D. Link, and J. A. Font, Classical and Quantum Gravity **27**, 114105 (2010), 1001.3074.

[16] C. Reisswig, R. Haas, C. D. Ott, E. Abdikamalov, P. Mösta, D. Pollney, and E. Schnetter, Phys. Rev. D **87**, 064023 (2013), 1212.1191.

[17] W. Tichy, Phys. Rev. D **86**, 064024 (2012), 1209.5336.

[18] W. Tichy, Classical and Quantum Gravity **26**, 175018 (2009), 0908.0620.

[19] P. Tsatsin and P. Marronetti, Phys. Rev. D **88**, 064060 (2013), 1303.6692.

[20] K. Taniguchi, T. W. Baumgarte, J. A. Faber, and S. L. Shapiro, Phys. Rev. D **75**, 084005 (2007), gr-qc/0701110.

[21] F. Foucart, M. B. Deaton, M. D. Duez, L. E. Kidder, I. MacDonald, C. D. Ott, H. P. Pfeiffer, M. A. Scheel, B. Szilagyi, and S. A. Teukolsky, Phys. Rev. D **87**, 084006 (2013), 1212.4810.

[22] F. Foucart, L. E. Kidder, H. P. Pfeiffer, and S. A. Teukolsky, Phys. Rev. D **77**, 124051 (2008), URL http://link.aps.org/doi/10.1103/PhysRevD.77.124051.

[23] K. Kyutoku, M. Shibata, and K. Taniguchi, Phys. Rev. D **79**, 124018 (2009), 0906.0889.

[24] S. Husa, M. Hannam, J. A. González, U. Sperhake, and B. Brügmann, Phys. Rev. D **77**, 044037 (2008), URL http://link.aps.org/doi/10.1103/PhysRevD.77.044037.

[25] J. M. Bowen and J. W. York, Jr., Phys. Rev. D **21**, 2047 (1980).

[26] R. Haas et al., Astrophys.J. **749**, 117 (2012), 1201.4389.

[27] J. Healy, T. Bode, R. Haas, E. Pazos, P. Laguna, D. M. Shoemaker, and N. Yunes, Classical and Quantum Gravity **29**, 232002 (2012), 1112.3928.

[28] T. Bode, P. Laguna, and R. Matzner, Phys. Rev. D **84**, 064044 (2011), 1106.1864.

[29] T. Bode, T. Bogdanovic, R. Haas, J. Healy, P. Laguna, et al., Astrophys.J. **744**, 45 (2012).

[30] T. Bode, R. Haas, T. Bogdanovic, P. Laguna, and D. Shoemaker, Astrophys. J. **715** (2010).

[31] J. Healy, J. Levin, and D. Shoemaker, Phys. Rev. Lett. **103**, 131101 (2009).

[32] T. W. Baumgarte and S. L. Shapiro, Phys. Rev. D **59**, 024007 (1999), gr-qc/9810065.

[33] M. Campanelli, C. O. Lousto, P. Marronetti, and Y. Zlochower, Phys. Rev. Lett. **96**, 111101 (2006).

[34] J. G. Baker, J. Centrella, D.-I. Choi, M. Koppitz, and J. van Meter, Phys.Rev.Lett. **96**, 111102 (2006), gr-qc/0511103.

[35] et-web, einstein Toolkit home page:http://www.einsteintoolkit.org.

[36] G. Allen, T. Goodale, and E. Seidel, in *7th Symposium on the Frontiers of Massively Parallel Computation-Frontiers 99* (IEEE, New York, 1999).

[37] E. Schnetter, S. H. Hawley, and I. Hawke, Class. Quant. Grav. **21**, 1465 (2004).

[38] S. Husa, I. Hinder, and C. Lechner, Computer Physics Communications **174**, 983 (2006).

[39] L. L. Smarr, ed., *Sources of gravitational radiation; Proceedings of the Workshop, Seattle, Wash., July 24-August 4, 1978* (1979).

[40] J. M. Bowen, General Relativity and Gravitation **11**, 227 (1979).

[41] M. Shibata and K. Taniguchi, Living Reviews in Relativity **14** (2011), URL http://www.livingreviews.org/lrr-2011-6.

[42] K. Oohara and T. Nakamura, Progress of Theoretical Physics **81**, 360 (1989).

[43] E. Kvaalen, BIT Numerical Mathematics **31**, 369 (1991), ISSN 0006-3835, URL http://dx.doi.org/10.1007/BF01931297.

[44] L. Baiotti, B. Giacomazzo, and L. Rezzolla, Phys. Rev. D **78**, 084033 (2008), 0804.0594.

[45] K. Hotokezaka, K. Kiuchi, K. Kyutoku, T. Muranushi, Y.-i. Sekiguchi, M. Shibata, and K. Taniguchi, Phys. Rev. D **88**, 044026 (2013), URL http://link.aps.org/doi/10.1103/PhysRevD.88.044026.

[46] L. Baiotti, B. Giacomazzo, and L. Rezzolla, Class. Quant. Grav. **26**, 114005 (2009), 0901.4955.

[47] S. Bernuzzi, T. Dietrich, W. Tichy, and B. Brügmann, Phys. Rev. D **89**, 104021 (2014), 1311.4443.

[48] M. Shibata, K. Kyutoku, T. Yamamoto, and K. Taniguchi, Phys. Rev. D **79**, 044030 (2009), URL http://link.aps.org/doi/10.1103/PhysRevD.79.044030.